

Dye visualization near a three-dimensional stagnation point: application to the vortex breakdown bubble

M. BRØNS¹†, M. C. THOMPSON^{2,3} AND K. HOURIGAN^{2,3}

¹Department of Mathematics, Technical University of Denmark, DK-2800 Lyngby, Denmark

²Fluids Laboratory for Aeronautical and Industrial Research (FLAIR), Department of Mechanical and Aerospace Engineering, Monash University, Melbourne, Victoria 3800, Australia

³Division of Biological Engineering, Monash University, Melbourne, Victoria 3800, Australia

(Received 7 December 2007 and in revised form 27 September 2008)

An analytical model, based on the Fokker–Planck equation, is constructed of the dye visualization expected near a three-dimensional stagnation point in a swirling fluid flow. The model is found to predict dye traces that oscillate in density and position in the meridional plane in which swirling flows are typically visualized. Predictions based on the model are made for the steady vortex breakdown bubble in a torsionally driven cylinder and compared with computational fluid dynamics predictions and experimental observations. Previous experimental observations using tracer visualization techniques have suggested that even for low-Reynolds-number flows, the steady vortex breakdown bubble in a torsionally driven cylinder is not axisymmetric and has an inflow/outflow asymmetry at its tail. Recent numerical and theoretical studies show that the asymmetry of the vortex breakdown bubble, and consequently its open nature, can be explained by the very small imperfections that are present in any experimental rig. Distinct from this, here it is shown that even for a perfectly axisymmetric flow and breakdown bubble, the combined effect of dye diffusion and the inevitable small errors in the dye injection position lead to the false perception of an open bubble structure with folds near the lower stagnation point. Furthermore, the asymmetries in the predicted flow structures can be remarkably similar to those observed in flow observations and computational predictions with geometric asymmetries of the rig. Thus, when interpreting dye-visualization patterns in steady flow, even if axisymmetric flow can be achieved, it is important to take into account the relative diffusivity of the dye and the accuracy of its injection.

1. Introduction

It is well known that the use of tracers such as dye in flow visualization can lead to misleading observations in the case of unsteady flows (Hama 1962; Kline 1969; Williams & Hama 1980; Cimbalá, Nagib & Roshko 1981, 1988; Kurosaka & Sundram 1986; Gursul, Lusseyran & Rockwell 1990; Gursul & Rockwell 1991). Apart from the distinction between streamlines and streaklines in unsteady flows, other problems related to the use of dye streaklines or fluid markers include the finite thickness of the marker, the difficulty of precisely defining the injection location of the marker, and

† Email address for correspondence: m.brons@mat.dtu.dk

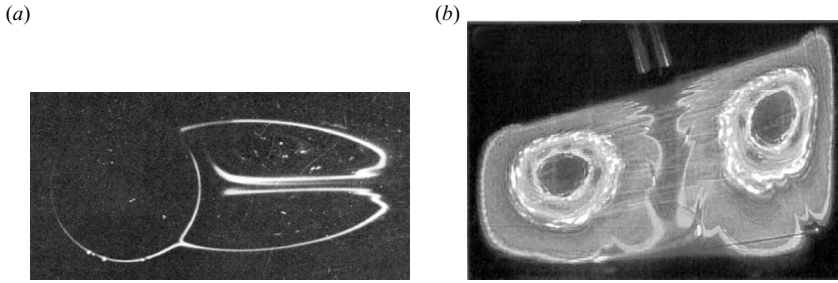


FIGURE 1. (a) Flow around a circular cylinder at Reynolds number 28.4 (with permission from Taneda 1956). (b) Experimental Poincaré section visualized with the use of continuously injected fluorescent dye streams for the flow below an impeller in a mixing tank (with permission from Fountain *et al.* 1998).

the mass diffusion of tracer reflected by the Schmidt number. Although the fallacies associated with streaklines in unsteady flows have been well documented, misleading visualizations involving steady flows are less common; it is generally assumed that they provide an accurate depiction of the flow structures.

In steady flows, stagnation points are known to lead to chaotic regions in which the trajectories of tracing particles separate exponentially fast; material filaments, tracked by, for example, dye, are stretched and folded continuously by means of horseshoes (Ottino *et al.* 1988). Folds in the dye visualization taken by Taneda (1956) for the steady flow around a circular cylinder (see figure 1a), are found near the downstream stagnation point of the recirculating region even before unsteadiness appears in the far wake. For swirling flows, the flow structures are usually captured by a plane cut using a laser sheet and the injection of fluorescent dye streams. The case of the flow in a tank having two hyperbolic fixed points in the region below an impeller has been studied by Fountain, Khakhar & Ottino (1998), revealing, within a Lagrangian description, chaotic structures with high-period islands. Of note in figure 1(b) are the folds in the dye streaks near both the downstream stagnation point on the impeller (top centre of image) and the upstream stagnation point (bottom centre of the image).

The local flow close to a stagnation point is well understood, and depends essentially on the eigenvalues of the linearization of the velocity field (Chong, Perry & Cantwell 1990; Bakker 1991; Brøns 2007). Complex flow patterns arise when the global structure of the velocity field includes a mechanism for re-injecting fluid particles which move away from a hyperbolic stagnation point back into a neighbourhood of the point. Such a mechanism will be provided by a homoclinic connection, a streamline or streamsurface connecting a hyperbolic stagnation point to itself, or, more generally, a heteroclinic connection which links several stagnation points in a closed chain. The complex motion arising when such structures occur in unsteady flow is analysed by Holmes (1984), Rom-Kedar, Leonard & Wiggins (1990) and Lopez & Perry (1992) and in three-dimensional steady flow by Hartnack, Brøns & Spohn (2000), Sotiropoulos & Ventikos (2001) and Brøns *et al.* (2007).

The study of the expected dye-visualization patterns near a stagnation point in a swirling flow is the focus of the first part of this paper. In the second part, the particular case of the stagnation point associated with a vortex breakdown is considered. Concerns over the problem of misleading visualization in the case of vortex breakdown were in fact noted by Delery (1994): ‘According to some investigators, the bubble type of breakdown would be the only basic configuration, the spiral and other

types being different images of the same phenomenon resulting from the visualization technique.'

There has been considerable debate in the literature since as to whether the recirculation region observed in the flow in a closed cylindrical container with a spinning lid should even be termed 'vortex breakdown' (Leibovich 1978, 1984, 1999; Krause & Liu 1989; Spall, Gatski & Ash 1990; Goldshtik & Hussain 1998). Broadly speaking, the recirculation pattern in the closed cylinder has appeared to be axisymmetric, non-hysteretic, closed and sometimes steady as opposed to the open, asymmetric, hysteretic and unsteady vortex breakdown structures observed in the flow over delta wings and in open vortex tubes.

Below a certain Reynolds number, Gelfgat, Bar-Yoseph & Solan (1996) have demonstrated numerically that the confined cylinder flow is stable with respect to axisymmetric perturbations up to moderate Reynolds numbers. At least in this lower-Reynolds-number range, the confined cylinder flow has appeared to be robustly axisymmetric with closed steady bubbles, with near-axis separation zones appearing gradually, and not discontinuously, as the control parameters are changed. Three-dimensional flow simulations at these lower Reynolds numbers have predicted axisymmetric vortex breakdown patterns except where asymmetries have been introduced, through, for example, flow or geometrical perturbations (Brøns 2007; Brøns *et al.* 2007), grid asymmetries (Sotiropoulos & Ventikos 2001; Sotiropoulos *et al.* 2001, 2002), dye density variations (Gelfgat 2002), or lid tilt (Thompson & Hourigan 2003).

Previously, Hourigan, Graham & Thompson (1995) have investigated the issue of whether steady small-scale spirals often observed in the pre-vortex breakdown region were due to unsteadiness or asymmetry in the flow in confined cylinders. The motivation in that study was to investigate whether the spirals that appeared were real flow structures, possibly related to wave trapping. The spirals also appear just upstream of the vortex breakdown in some situations. It was demonstrated that the spirals could also be an artefact of the dye-visualization technique, resulting from imperceptibly small offsets of the dye injection from the central axis of the cylinder. In the case of a developed vortex breakdown, Sotiropoulos *et al.* (2002) state that: 'Axisymmetric streamlines, of course, cannot reproduce the asymmetric dye-tracer patterns observed in the laboratory.' In the present paper, we will demonstrate that the combined effect of diffusion and misalignment of tracer injection will lead to a dye distribution which deviates significantly from that predicted from the streamline pattern, and that asymmetries may appear even if the flow field is perfectly axisymmetric.

Determining the flow structures and mixing properties of the flow in a confined cylinder has assumed a further practical importance for cell culture and tissue engineering since the initial experimental investigations (Dusting, Sheridan & Hourigan 2004, 2006), computational studies (Yu *et al.* 2005*a,b*, 2007; Tan *et al.* 2006; Liow *et al.* 2007) and cell culture (Thouas, Sheridan & Hourigan 2007). To exploit the idea of the vortex breakdown bubble being a 'virtual reactor' in which constructs such as scaffolds could be placed or cells cultured, the issue of whether the bubble is closed or open, symmetrical or asymmetrical, becomes all the more important.

In this paper, we demonstrate how, through a combination of mass diffusion of the tracer fluid and the error in the tracer injection location, not only can 'asymmetric' and 'open' structures appear for a steady purely axisymmetric flow involving vortex breakdown, but the structures can appear to be remarkably similar to those observed

experimentally. In a dye-visualization experiment, this effect will appear in addition to the complexity of the flow which stems from geometric imperfections. The first part of the paper examines this behaviour from theory, based on the Fokker–Planck equation. In particular, the behaviour in the neighbourhood of the downstream hyperbolic point is modelled asymptotically. The second part of the paper attempts to quantify the effects of tracer diffusion and minor off-axis injection on the observed appearance of otherwise axisymmetric breakdown.

2. An analytical model for dye distribution near a stagnation point

2.1. The Fokker–Planck equation

To explore the distribution of dye at the downstream part of a steady vortex breakdown bubble, we study the flow in the vicinity of the stagnation point that constitutes the end-point of the bubble on the cylinder axis. In a region close to a stagnation point, the velocity field can be approximated by its linearization. We define an xyz coordinate system with origin at the stagnation point and the z -axis along the cylinder axis and consider the linearization

$$\mathbf{v}(\mathbf{r}) = \mathbf{A}\mathbf{r}, \quad (2.1)$$

where \mathbf{A} is the Jacobian matrix of the full velocity field. Assuming the flow has axial symmetry, we have

$$\mathbf{A} = \begin{pmatrix} -\alpha & \beta & 0 \\ -\beta & -\alpha & 0 \\ 0 & 0 & 2\alpha \end{pmatrix}, \quad (2.2)$$

where

$$\alpha = -\frac{\partial u}{\partial x} = -\frac{\partial v}{\partial y}, \quad \beta = \frac{\partial u}{\partial y} = -\frac{\partial v}{\partial x} \quad (2.3)$$

are derivatives evaluated at the stagnation point. With $\alpha > 0$, the (x, y) -plane is the stable manifold W^s of the stagnation point, consisting of streamlines which spiral around the axis with angular velocity β (swirl) and are attracted exponentially with a rate α to the stagnation point. The surface W^s is the linear approximation of the lower part of the bubble surface. Streamlines starting off W^s will also perform a spiralling motion, but will be repelled from W^s along the unstable manifold W^u , the z -axis (figure 2). An analogous structure, but with $\alpha < 0$, exists close to the upstream stagnation point. A more detailed description of the flow field in vortex breakdown has been obtained by Rusak (1996).

We model the motion of the dye as a standard Brownian motion superimposed on the drift given by the linearized velocity field, i.e. by the stochastic or Langevin differential equation

$$\frac{d\mathbf{r}}{dt} = \mathbf{A}\mathbf{r} + \epsilon\boldsymbol{\Gamma}(t). \quad (2.4)$$

Here, $\boldsymbol{\Gamma}(t)$ is a vector of independent Gaussian distributions $\Gamma_i(t)$ with zero mean and unit variance,

$$\langle \Gamma_i(t) \rangle = 0, \quad \langle \Gamma_i(t)\Gamma_j(t') \rangle = \delta_{ij}\delta(t-t'), \quad (2.5)$$

(see Risken 1989). Here, $\langle \cdot \rangle$ denotes expectation value. The parameter ϵ is the r.m.s. noise level. The probability density p for a particle is governed by the associated Fokker–Planck or forward Kolmogorov equation (Risken 1989; Gardiner 1985). This

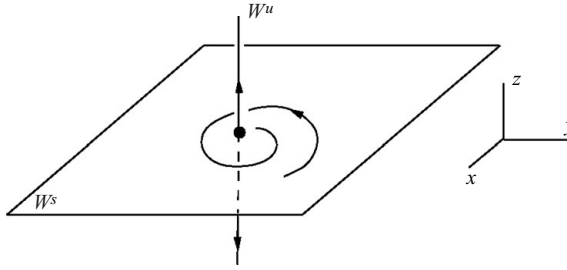


FIGURE 2. The basic geometry of the flow structure close to the stagnation point showing the stable manifold W^s (the linear approximation of the lower part of the bubble surface) with a typical streamline spiralling inward and the unstable manifold W^u (the cylinder axis.)

is the diffusion equation

$$\frac{\partial p}{\partial t} = -\nabla \cdot (\mathbf{A}\mathbf{r}p) + \frac{\epsilon^2}{2} \Delta p. \quad (2.6)$$

The parameter ϵ is connected to the Schmidt number as follows: the Schmidt number is the ratio of the diffusivities of the fluid and the dye, i.e.

$$Sc = \frac{\nu}{\epsilon^2/2} = \frac{2}{\epsilon^2 Re}, \quad (2.7)$$

where the latter identity holds when dimensionless variables are used.

We denote the solution to the Fokker–Planck equation (2.6) where the particle is located at $\mathbf{r}_0 = (x_0, y_0, z_0)$ at $t = t_0$ by $p = p(\mathbf{r}, t | \mathbf{r}_0, t_0)$, i.e. the solution which fulfils the initial condition $p(\mathbf{r}, t_0 | \mathbf{r}_0, t_0) = \delta(\mathbf{r} - \mathbf{r}_0)$. This solution is a multi-dimensional Gaussian distribution (Risken 1989)

$$p(\mathbf{r}, t | \mathbf{r}_0, t_0) = \frac{1}{(2\pi)^{3/2} \sqrt{\det \Sigma}} \exp\left(-\frac{1}{2}(\mathbf{r} - \boldsymbol{\mu})^T \Sigma^{-1}(\mathbf{r} - \boldsymbol{\mu})\right). \quad (2.8)$$

Here, the mean value evolves according to the deterministic velocity field given by (2.1),

$$\boldsymbol{\mu} = \exp(\mathbf{A}(t - t_0))\mathbf{r}_0. \quad (2.9)$$

The exponential matrix is

$$\exp(\mathbf{A}t) = \begin{pmatrix} \exp(-\alpha t) \cos \beta t & -\exp(-\alpha t) \sin \beta t & 0 \\ \exp(-\alpha t) \sin \beta t & \exp(-\alpha t) \cos \beta t & 0 \\ 0 & 0 & \exp(2\alpha t) \end{pmatrix}, \quad (2.10)$$

and the variance is

$$\begin{aligned} \Sigma &= \int_{t_0}^t \epsilon^2 \exp(\mathbf{A}(\tau - t_0)) \exp(\mathbf{A}^T(\tau - t_0)) d\tau \\ &= \epsilon^2 \begin{pmatrix} \frac{1 - \exp(-2\alpha(t - t_0))}{2\alpha} & 0 & 0 \\ 0 & \frac{1 - \exp(-2\alpha(t - t_0))}{2\alpha} & 0 \\ 0 & 0 & \frac{\exp(4\alpha(t - t_0)) - 1}{4\alpha} \end{pmatrix}. \end{aligned} \quad (2.11)$$

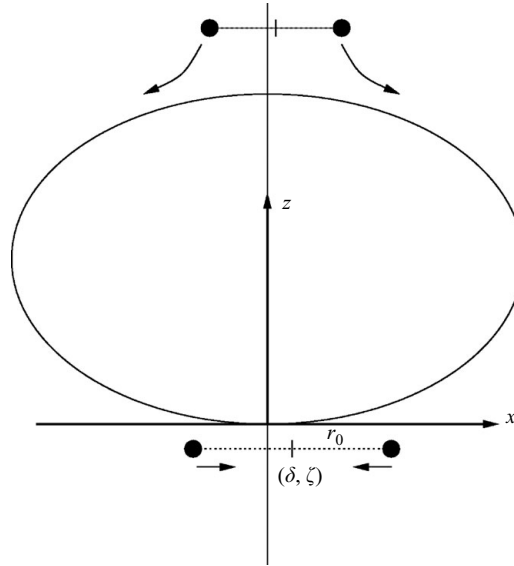


FIGURE 3. Sketch of the flow of tracer particles around the breakdown bubble. A meridional intersection is shown. A circle of tracer particles is released above the bubble, slightly displaced from the cylinder axis. The circle will expand as it is attracted to the bubble surface, and during this phase diffusion is ignored. When the lower part of the bubble is reached, the downstream stagnation point is approached as the circle shrinks again. At some stage, taken as the initial time in the analysis, the particles form a circle of radius r_0 . The circle is still displaced from the axis and is outside the bubble. In the coordinate system centred at the lower stagnation point, the centre has coordinates (δ, ζ) with $\zeta < 0$.

2.2. Application to dye release in a visualization experiment

The probability density of a single tracer particle is given by (2.8). To model the distribution of dye in a vortex breakdown experiment, consider the flow of particles released in a single horizontal circle above the breakdown bubble with the centre slightly displaced from the axis (see figure 3). This circle of particles will be attracted to the bubble surface while the radius increases as it flows out along the top of the bubble surface. Assuming that diffusion is negligible during this stage of the flow, the circle will stay outside the breakdown bubble. After a certain time, the circle will have reached the lower part of the bubble surface, and, as the radius now decreases, it enters the region where the linearization (2.1) is valid. At the entry to this stage, we assume that the particles still constitute a circle of the form

$$\mathbf{r}_c = (r_0 \cos \theta + \delta, r_0 \sin \theta, \zeta), \quad \theta \in [0, 2\pi]. \quad (2.12)$$

As the particles are below the bubble surface, $\zeta < 0$. Both ζ and δ , which measure the off-axis displacement of the particles from the axis, will be taken as small parameters.

If the particles are uniformly distributed on the circle (2.12) at time t_0 , the total density of particles at $t > t_0$ is

$$\rho_c(\mathbf{r}, t | \mathbf{r}_c, t_0) = \int_0^{2\pi} p(\mathbf{r}, t | \mathbf{r}_c, t_0) d\theta. \quad (2.13)$$

Since not only a single circle of particles is released, but this release goes on continuously from, say, $t = 0$, the total density of particles is

$$\rho(\mathbf{r}, t) = \int_0^t \rho_c(\mathbf{r}, t | \mathbf{r}_c, t_0) dt_0. \quad (2.14)$$

In particular, an equilibrium density will appear in the limit $t \rightarrow \infty$,

$$\rho_\infty(\mathbf{r}) = \int_0^\infty \rho(\mathbf{r}, t) dt. \quad (2.15)$$

Since the integrals (2.13) and (2.14) involve normal distributions, the saddle-point method (de Bruijn 1970) may in some cases be used to obtain analytical approximations for small ϵ . Here, we consider the density of particles along the bubble surface $z = 0$ in a Poincaré plane which we choose as $y = 0$. The derivation can be found in the Appendix. We find to lowest order in the small parameters δ , ζ

$$\begin{aligned} \rho_\infty(x, 0, 0) = \frac{1}{\epsilon} \sqrt{\frac{2}{\pi\alpha}} \frac{1}{\sqrt{r_0^4 - x^4}} \left[1 + \frac{\text{sign}(x)}{r_0} \left\{ \frac{r_0^4 + x^4}{r_0^4 - x^4} \cos \left[\frac{\beta}{\alpha} \ln \left(\frac{|x|}{r_0} \right) \right] \right. \right. \\ \left. \left. + \frac{\beta}{\alpha} \sin \left[\frac{\beta}{\alpha} \ln \left(\frac{|x|}{r_0} \right) \right] \right\} \delta - \frac{2r_0^4\alpha}{r_0^4 - x^4} \left(\frac{\zeta}{\epsilon} \right)^2 \right] \end{aligned} \quad (2.16)$$

for $x \neq 0$. Since the flow field (2.1) is symmetric in z , only terms of even order in ζ appear in the Taylor expansion of ρ_∞ .

If particles are released symmetrically with respect to the cylinder axis, i.e. $\delta = 0$, the equilibrium density is also symmetric. However, if $\delta \neq 0$, a pattern of high and low dye densities occurs. If x/r_0 is not too large such that

$$\frac{r_0^4 + x^4}{r_0^4 - x^4} \approx 1, \quad (2.17)$$

it is easy to see there is a sequence of local maxima $x_n \rightarrow 0$ of ρ_∞ which form a geometric progression,

$$x_{n+1} = \exp\left(-2\pi\frac{\alpha}{\beta}\right) x_n, \quad (2.18)$$

and, correspondingly, a sequence of minima in-between the maxima with the same distribution. If a single particle were released in the velocity field (2.1) with no diffusion present, the relation (2.18) would hold exactly for the subsequent crossings of a meridional plane. In the present model, this is slightly modified when (2.17) does not hold, but the density pattern is independent of the diffusivity ϵ . Furthermore, this pattern depends only on the fluid velocity field through the ratio α/β , and the displacement δ contributes only to the amplitude of the density variations, not to the wavelength of density variations.

The maxima x_n of the density accumulate on the axis, and the approximation (2.16) hence predicts an infinite number of oscillations with a wavelength tending to zero as the axis is approached. However, for a fixed ϵ , the saddle-point approximation is accurate only when the integrand is sufficiently located. As time increases and the probability density of an individual particle is smeared out, the approximation breaks down. As the particles that reach small values of x have travelled a long time (see (A 10)), the expression (2.16) is not accurate for small x . This is illustrated in figure 4 for values of the parameters which are relevant for the vortex breakdown,

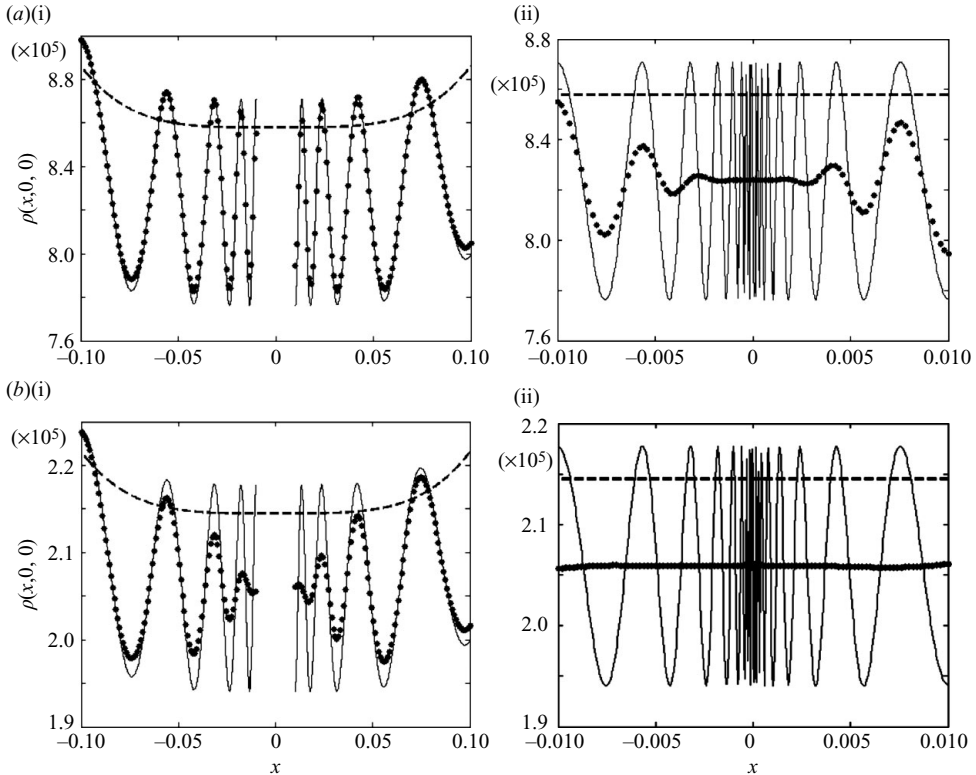


FIGURE 4. Equilibrium particle density $\rho_\infty(x, 0, 0)$ as a function of the coordinate x for $\alpha = 0.02$, $\beta = 0.22$, $r_0 = 0.25$, $\delta = 0.001$, $\zeta/\epsilon = -1$, for different values of the diffusivity ϵ . (i) show results away from the axis; (ii) show the details near the stagnation point at the origin. (a) Schmidt number 4.0×10^4 ; (b) 2.5×10^5 . The full line is the analytical approximation (2.16). The markers show numerical computations of the full integral (2.14). The dashed line is the analytical approximation (2.16) with no perturbation, $\delta = \zeta = 0$.

see §3.3, where it also appears that the analytic approximation is more accurate for smaller ϵ .

The present analysis is concerned with the flow close to the lower stagnation point of the bubble. A similar analysis could be performed near the top stagnation point, where the essential change is that $\alpha < 0$. The analysis would describe how particles flow along the top part of the bubble which is attracting and how non-uniformities in that distribution will evolve. The key to the sensitivity in the breakdown bubble is the stable two-dimensional manifold W^S near the lower stagnation point which separates particles that go up and into the bubble from particles which go down and out of the bubble. There is no similar structure near the top stagnation point. This will appear clearly in the figures in §3.4 where it can be seen that the depicted shape of the top part of the bubble is very robust against misalignment of dye injection.

3. Numerical studies of dye traces and experimental comparisons

3.1. Numerical approach

The strategy employed to investigate the visualization of tracers by numerical means was as follows. First, the purely axisymmetric base fluid flow was predicted using a

Galerkin finite-element method. Then numerical particles representing the tracer were projected onto the steady flow solution through their introduction near the top of the confined cylinder, convected following the streamlines of the base flow plus a random walk to mimic mass diffusion. More details are provided below.

3.2. Finite-element method

The Galerkin finite-element method was used to obtain the solution of the Navier–Stokes equations for axisymmetric flow in cylindrical coordinates. The numerical mesh consisted of uniform rectangular elements except for a sinusoidal compression of the first five elements near the rotating lid in order to capture the boundary layers including the Ekman layer. The penalty formulation with biquadratic Lagrangian interpolation (9-node quadratic quadrilateral elements) for the velocity field and under-integration of the continuity constraint was employed (Zienkiewicz 1977). Formally, this method leads to a third-order accurate velocity field and this has been verified by careful convergence studies. The nonlinear set of equations was solved by Newton iteration, with the stopping criterion being when the L_2 -norm of the velocity differences was less than 10^{-6} . The code has been tested successfully against a variety of benchmark problems, including driven cavity, backward-facing step and flow around a circular cylinder, and previously for the torsionally driven cylinder (Hourigan *et al.* 1995). In addition, resolution studies using a series of meshes of increasing fineness verified that the global solution error in the velocity field was better than 0.1 %.

3.3. Tracer diffusivity

Numerical experiments simulating dye tracing were then undertaken by introducing particles near the centre of the top non-spinning lid. This mimics the way dye traces are typically introduced into flows. The motion of the dye is found by simulating the Langevin equation which appears when the full velocity field is replacing the linearization in (2.4). In each time step, a Gaussian distributed random walk is added. The variance σ^2 of the random walk is related to the time step Δt and the r.m.s. level ϵ by $\sigma^2 = \epsilon^2 \Delta t$ (Ghoniem & Sherman 1985). From this, a molecular Schmidt number ($Sc =$ ratio of momentum diffusivity to mass diffusivity) can be calculated. In the three-dimensional computations, the tracer particles are released randomly within a small circular cross-section, analogous to dye injection or precipitated particle generation in the experiments. The time integration of particle positions is performed using the standard second-order Adams–Bashforth method. The fluid velocity at particle positions is calculated using polynomial interpolation corresponding to the finite-element discretization, thereby retaining the spatial accuracy of the velocity field solution within mesh elements, not just at nodal points. The time step is sufficiently small that the particle paths accurately trace out the streamlines of the flow when the random walk component is switched off. The random walk algorithm is tested in a uniform axial flow with a Gaussian initial distribution of particles, where an analytical solution can be obtained. Excellent agreement is obtained.

The effect of the two parameters on the visualization results was quantified in this study: the offset of the injection point relative to the central axis of the cylinder; and the mass diffusivity (or Schmidt number) of the tracer in the fluid.

3.4. Results and discussion

The main hypothesis to be tested is that even for a purely steady axisymmetric flow field, namely the closed bubble of vortex breakdown in a torsionally driven cylinder,

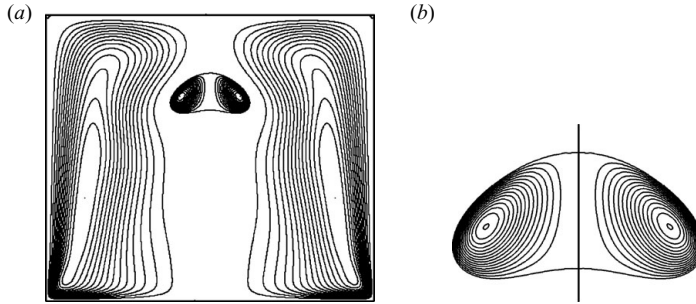


FIGURE 5. The streamlines of predicted axisymmetric flow for Reynolds number 1850 and aspect ratio 1.75. (a) Full diametral plane; (b) the enlarged view of the recirculation bubble with centreline axis.

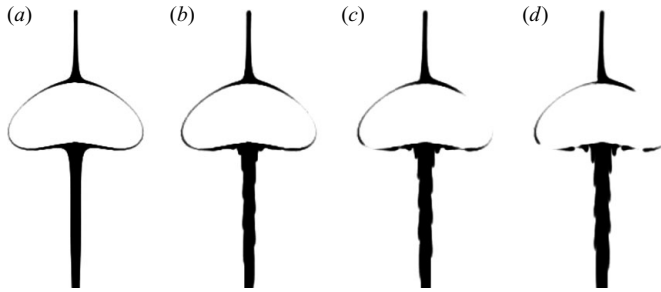


FIGURE 6. The particle trace plots as the offset of dye introduction from the centreline is increased: (a) no offset, (b) offset = $0.000625D$, (c) offset = $0.00125D$, (d) offset = $0.001875D$. Zero mass diffusion, $Re = 1850$, aspect ratio 1.75.

seemingly quite carefully implemented passive tracer visualization can suggest that the bubble is open and asymmetrical.

The flow field was predicted for a Reynolds number of 1850 and an aspect ratio of 1.75, after Spohn, Mory & Hopfinger (1998). The Reynolds number is defined as $Re = \Omega R^2/\nu$, where Ω is the angular velocity of the rotating cover, R is the radius of the cylinder, and ν is the viscosity of the fluid. The streamline pattern of the predicted axisymmetric flow is shown in figure 5. A recirculation bubble is found on the central axis, similar in general shape to that observed experimentally except that it has a closed form and is constrained to be purely axisymmetric.

The effect of feeding in tracer particles from a circular cross-section offset from the central axis was then investigated. First, the tracer particles were allowed to follow the streamlines of the general flow. The offset of the circular cross-section through which particles were released was varied between 0 and 0.001875 times the cylinder diameter, D . Particles are only plotted when they lie in the range $-0.0025D \leq y \leq 0.0025D$, to mimic the way fluorescent dye images are often taken with a thin laser sheet. Here, y is the coordinate into the page. The predicted visualization patterns are shown in figure 6. When the tracer particles are released from within a circle, of radius $0.0025D$, concentric with the cylinder, the predicted flow pattern of the tracer is symmetrical everywhere in the flow (see figure 6a). However, offsetting the particle release positions by even minute amounts is seen to introduce an increasingly distinct asymmetry to the flow, although the bubble remains closed.

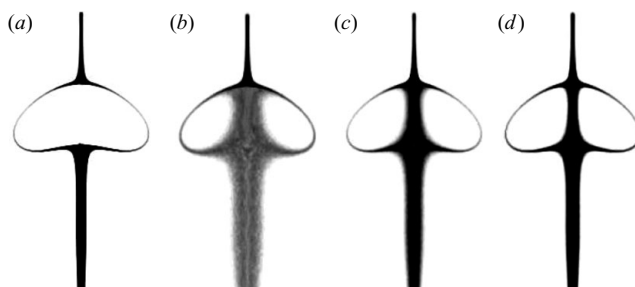


FIGURE 7. Plots showing the effect of tracer mass diffusivity (a) $Sc = \infty$, i.e. no diffusion, (b) $Sc = 2000$, (c) 20 000, (d) 200 000. There is no offset of injection from the central axis. $Re = 1850$, aspect ratio 1.75.

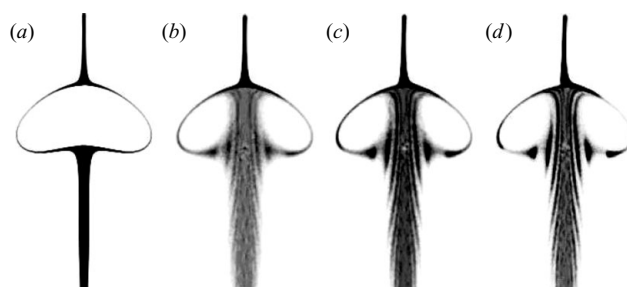


FIGURE 8. Plots showing the combined effect of tracer diffusion ($Sc = 2000$) and dye offset, (a) no diffusion or offset, (b) offset = $0.00125D$, (c) $0.0025D$ (d) $0.00375D$. $Re = 1850$, aspect ratio 1.75.

Next, the independent effect of introducing a mass diffusivity (i.e. different Schmidt number) of the tracer material was investigated in the case of a zero offset of the tracer particle introduction (figure 7). As the tracer Schmidt number is decreased, particles are increasingly able to ‘diffuse’ across the closed streamlines around the recirculation bubble, both into and out of the breakdown region. Additional diffusivity of the tracer produces the image of an increasingly open vortex breakdown bubble. Note that the appearance of the visualizations is somewhat affected by details of the numerical imaging method. Here, the particle positions are recorded as they pass through the domain and the image is constructed by mapping the positions to a discrete 512×512 pixel image. The image brightness (or darkness) at each pixel position is obtained summing the contributions of nearby particles assuming each has an associated Gaussian density distribution. This allows for some image smoothing. Nevertheless, despite using 10 000–20 000 tracer particles for each image, and because the particle positions are only captured when they pass through a small imaging window, the images are still somewhat grainy, especially for the most diffusive case $Sc = 2000$.

When the effects of dye offset and diffusivity are combined, it is possible to reproduce features of the asymmetrical and open bubbles observed experimentally. The predicted tracer particle distributions for successive times in the case of combined non-zero injection offset and tracer mass diffusivity are shown in figure 8. The time-dependent formation of the dye-visualization is shown in figure 9.

The effect of a small and a larger dye injection offset predicted numerically, compared with the observations of Spohn *et al.* (1998), and with Sotiropoulos *et al.*

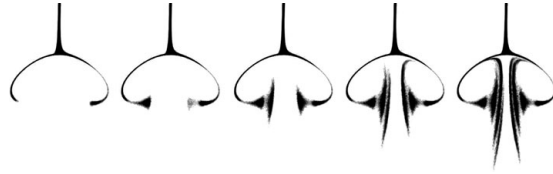


FIGURE 9. Diametral view of predicted tracer pattern at successive stages of numerical tracer entering the vortex breakdown region. $Re = 1850$, aspect ratio = 1.75, dye offset = $0.0025D$, $Sc = 2000$.

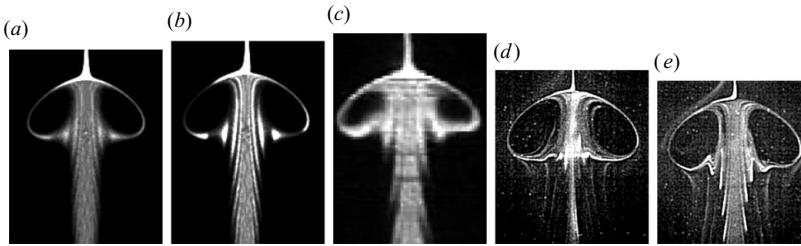


FIGURE 10. Simulation with (a) offset = $0.00125D$ and (b) $0.00375D$. $Re = 1850$, aspect ratio = 1.75, $Sc = 2000$. (c) Dye visualization of Spohn *et al.* (1998). (d) Dye visualization of Sotiropoulos *et al.* (2002), no lid tilt and (e) lid tilt, showing the apparently open bubble at $Re = 1850$, aspect ratio 1.75.

(2002) for different lid tilts, is shown in figure 10. The common features, for both lid tilt and no intended lid tilt, are the open nature of the bubbles and the asymmetry of bubbles with alternating folds in the dye patterns.

Spohn *et al.* (1998) note that that, ‘Neither in the horizontal plane adjacent to the cover, nor in a vertical diametral plane can we see any asymmetries. Clearly the electrolytic precipitation supplied tracer particles in a highly axisymmetric way.’ We have shown by the current study and the previous one on pre-vortex breakdown spirals (Hourigan *et al.* 1995) that even a ‘highly axisymmetric way’ may not be sufficiently axisymmetric to avoid an asymmetric trace. By definition, a vortex breakdown bubble involves the rapid and relatively massive dilation of streamlines; that is, the radial expansion of streamlines away from the central axis can be large. Therefore, even asymmetries in the streaklines that are imperceptible to the eye are amplified to significant magnitudes at the breakdown bubble.

The behaviour seen in figures 6–9 is described well by the theory of §2.2. The wavelength of the dye density pattern is independent of the dye offset (figure 8), which is modelled by the parameter δ in (2.16). Only the amplitude of the density variation increases with dye injection offset, making the pattern more clearly visible for larger offsets. To further validate the model quantitatively, we have tested the predictions of the theoretical model against the directly measured density variation from the numerical simulations. To do this, we have found the radial variation of the equilibrium particle density along a meridional intersection of the lower breakdown bubble surface, corresponding to $\rho_\infty(x, 0, 0)$, equation (2.16). This is done by finding the number of particles in each radial increment of a thin axial slice and dividing by the volume increment to give an estimate of the local particle density. The resulting distributions shown in figure 11 should be compared with similar theoretical plots in figure 4. The amplitude further away from the stagnation point is approximately constant, consistent with the theory. The initial decrease in amplitude closer to the

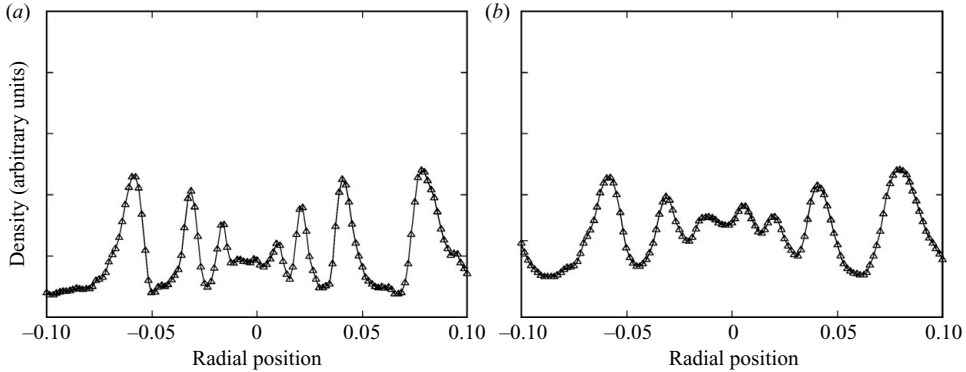


FIGURE 11. Numerically obtained distribution of dye along the lower part of the breakdown bubble for $Re = 1850$ and aspect ratio 1.75. (a) $Sc = 10^5$; (b) $Sc = 10^4$. Dye offset is $0.001R$.

stagnation point is caused by the finite axial width of the slice. Moving radially inwards towards the stagnation point, the amplitude of the oscillation shown in figure 6(d) progressively increases, so that some particles are not included in the integration volume. In fact close to the centre, particles are spread over a large axial distance and hence the particle density falls to low levels at the origin.

According to (2.18), the ratio x_{n+1}/x_n of consecutive maxima (and minima) is asymptotically constant with the value $\exp(-2\pi\alpha/\beta)$ for $x_n \rightarrow 0$. Computing this constant from the data in figure 11 from the peaks closest to the origin, we find the values 0.54 and 0.52, respectively. This compares well with the constant computed from the numerically obtained velocity field, where we obtain the value 0.52. Computing the ratio x_{n+1}/x_n for all the peaks shown shows a very small variation, even quite far from the axis, and we find the average values 0.51 ± 0.07 for $Sc = 10^5$ and 0.46 ± 0.07 for $Sc = 10^4$. It is not obvious that this accurate quantitative agreement should hold except at close to the stagnation point. The theory is based on a linearization at the cylinder axis, and we have obtained no estimates of how far out along the bubble surface it is a valid approximation. However, the variation of the angular velocity is less than 25% out to 40% of the bubble radius, which is consistent with the validity of the linearization extending quite far away from the stagnation point. Furthermore, even if a nonlinear correction of (2.18) was obtained giving a more precise estimate of the distribution of concentration peaks away from the stagnation pattern, the present analysis captures the essentials of the mechanism behind the pattern formation.

We conclude this section by showing some results for other values of the system parameters. Figure 12 shows the decisive parameter α/β as a function of Re for aspect ratio 1.75. The parameter shows only a small variation, which is reflected in the dye patterns shown in figure 13(a–c). In all cases, the distribution of dye near the lower stagnation point has very comparable wavelengths, even if the overall bubble shape changes significantly.

In figure 13(d), a case with two breakdown bubbles is shown. While the dye pattern close to the lower stagnation point of the top bubble is in agreement with the previous cases, the dye close to the lower stagnation point of the lower bubble appears to be homogeneously distributed. This is not surprising. First of all, the flow of the dye as it passes the top bubble results in a significant spread, and the injection relative to the lower bubble is quite different from that assumed in the model. Furthermore, for the lower bubble $\alpha/\beta = 0.045$, which is much less than the value for the top bubble.

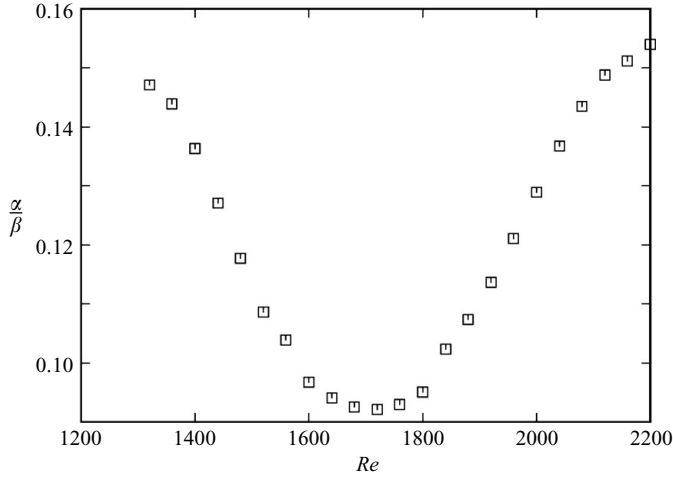


FIGURE 12. Variation of the parameter α/β at the lower stagnation point as a function of Re for aspect ratio 1.75.

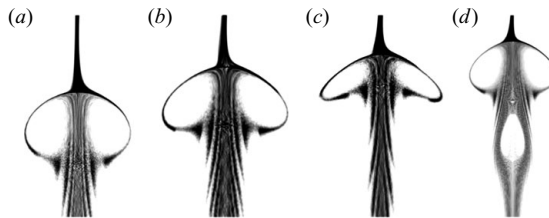


FIGURE 13. (a–c) Dye patterns for aspect ratio 1.75 and $Re = 1550, 1850, 2150$, respectively. (d) Aspect ratio 2.0, $Re = 2060$. In all cases, $Sc = 10^4$. Dye offset is $0.0125D$.

Thus, the swirl is much higher around the lower bubble, and this gives rise to a much smaller separation of windings according to (2.18). That is, any structure in the dye distribution that may have survived the transport through the top bubble will be smeared out.

4. Conclusions

Although a number of cases have been documented previously where streamlines and streaklines differ in unsteady flows, we have shown here that this can occur also in a steady flow. Tracer fluid can be transported across otherwise forbidden dividing streamlines as a result of mass diffusion. In the particular case of a vortex breakdown bubble, this can make the bubble appear to be an ‘open’ rather than ‘closed’ structure. The addition of even a minute offset from the central axis to the introduction of the ‘dye’ resulted further in an apparent asymmetry of the flow.

Experimental observations of asymmetric and open vortex breakdown bubbles can be reasonably reproduced by computational simulation even in a purely axisymmetric flow field. An analytical model, based on the Fokker–Planck equation, is found to predict well the density variations of the dye visualization expected near the downstream three-dimensional stagnation point of the vortex breakdown bubble. The model shows that, to lowest order in the Schmidt number and the dye injection offset,

the structure of the pattern depends only on the ratio of the axial expansion rate α and the swirl β at the lower stagnation point of the breakdown bubble.

Imperfections in rigs have been shown previously to lead to asymmetrical and open vortex breakdown patterns. This is an inherent and unavoidable effect which will occur in any experiment. The present work shows that, on top of this effect, dye injection may produce patterns which are artefacts of the visualization technique. Geometrical imperfections give rise to a highly complex flow. Not only does the bubble fold asymmetrically, the interior of the bubble is filled with a nested structure of KAM tori and chaotic regions. These are, however, not generally available from a visualization experiment. In the standard set-up we have discussed here, dye is released above the breakdown bubble, and hence visualizes only the bubble surface. We have shown that an asymmetric bubble shape may occur solely because of diffusion, and hence describes well the experimental findings. However, a complex pattern inside the bubble will not occur because of dye diffusion alone. This will require some asymmetry of the rig. We do not consider diffusion of dye as an alternative explanation of a complex breakdown bubble structure to the well-established effect of geometrical imperfections, but as an independent physical effect. In a given experiment, both imperfections and diffusion will be present, and it is difficult to assess which will be the most important.

The main conclusion from the current study is that even if a perfect experimental rig could be constructed, visualization techniques using dye will probably result in the observation of asymmetrical and open vortex breakdown bubbles. This conclusion can be logically extended to other flows with hyperbolic critical points which will cause substantial amplification of perturbations as dye advects towards the stagnation point.

The authors gratefully acknowledge the funding from Australian Research Council Discovery Grant (DP0452664) and Linkage International Grant (LX0668992) for supporting this research. This research was conducted while M. B. was on a sabbatical leave at Monash University. The hospitality and excellent working conditions provided are gratefully acknowledged.

Appendix. Saddle-point approximations

Here, we briefly sketch how the approximation (2.16) is obtained. Let the functions g, h be defined on an interval I and let x_0 be a quadratic maximum for h ($h'(x_0) = 0, h''(x_0) < 0$) in the interior of I . Then asymptotically, as $\epsilon \rightarrow 0^+$, the saddle point method yields

$$\int_I g(x) \exp\left(\frac{h(x)}{\epsilon^2}\right) dx = \epsilon g(x_0) \sqrt{-\frac{2\pi}{h''(x_0)}} \exp\left(\frac{h(x_0)}{\epsilon^2}\right), \quad (\text{A } 1)$$

which is independent of the size of the interval I (de Bruijn 1970).

Since the dynamics (2.4) is not explicitly time-dependent, we have

$$p(\mathbf{r}, t | \mathbf{r}_0, t_0) = p(\mathbf{r}, t - t_0 | \mathbf{r}_0, 0). \quad (\text{A } 2)$$

From this it follows that

$$\rho(\mathbf{r}, t) = \int_0^t \rho_c(\mathbf{r}, t | \mathbf{r}_c, t_0) dt_0 = \int_0^t \rho_c(\mathbf{r}, \tau | \mathbf{r}_c, 0) d\tau, \quad (\text{A } 3)$$

and hence it suffices to consider the release time $t_0 = 0$ only.

We first approximate the integral (2.13). This has the form (A 1) with

$$h(\theta) = -\frac{\alpha}{1 - \exp(-2\alpha t)} \left(\{x - e^{-\alpha t} [r_0 \cos(\beta t + \theta) - \delta \cos(\beta t)]\}^2 + e^{-2\alpha t} \{r_0 \sin(\beta t + \theta) + \delta \sin(\beta t)\}^2 \right), \quad (\text{A } 4)$$

which is independent of ζ and

$$g = \frac{1}{\epsilon^3} \left(\frac{\alpha}{\pi} \right)^{3/2} \frac{\exp\left(\frac{2\alpha}{1 - e^{-4\alpha t}} (\zeta/\epsilon)^2\right)}{(1 - e^{-2\alpha t}) \sqrt{e^{4\alpha t} - 1}}, \quad (\text{A } 5)$$

which is independent of the integration variable θ . For $x > 0$, the maximum of h is attained, to first order in δ , at

$$\theta_0 = -\beta t - \frac{e^{-\alpha t} \sin(\beta t)}{x} \delta, \quad (\text{A } 6)$$

while for $x < 0$ it is

$$\theta_0 = \pi - \beta t - \frac{e^{-\alpha t} \sin(\beta t)}{x} \delta. \quad (\text{A } 7)$$

We consider first $x > 0$. Inserting in (A 1) and expanding to first order in δ , an approximation of ρ_c is obtained. Inserting this in (2.14), an integral of the form (A 1) is again obtained with

$$h(t) = \frac{2\alpha}{1 - e^{-4\alpha t}} \left(\frac{\zeta}{\epsilon} \right)^2 - \alpha \frac{((x - e^{-\alpha t} r_0)^2 - 2\delta \cos(\beta t) e^{-\alpha t} (x - r_0 e^{-\alpha t}))}{1 - e^{-2\alpha t}} \quad (\text{A } 8)$$

and

$$g(t) = \frac{\sqrt{2}\alpha}{\epsilon^2 \pi} \frac{1}{\sqrt{e^{2\alpha t} - 1} \sqrt{1 - e^{-4\alpha t}} \sqrt{r_0 x e^{\alpha t}}} \left(1 + \frac{\cos(\beta t)}{2x e^{\alpha t}} \delta \right). \quad (\text{A } 9)$$

The maximum of h is, to lowest order in the parameters, located at

$$t_0 = \frac{1}{\alpha} \ln \left(\frac{r_0}{x} \right) + \frac{1}{\alpha r_0} \cos \left(\frac{\beta}{\alpha} \ln \left(\frac{r_0}{x} \right) \right) \delta + \frac{1}{\alpha} \frac{4r_0^2 x^2}{r_0^4 - x^4} \zeta^2. \quad (\text{A } 10)$$

Applying the saddle-point approximation, the formula (2.16) follows for $x > 0$. The entire procedure is repeated for $x < 0$, yielding identical computations except for some changes of sign, and (2.16) results.

REFERENCES

- BAKKER, P. G. 1991 *Bifurcations in Flow Patterns*. Kluwer.
- BRØNS, M. 2007 Streamline topology – patterns in fluid flows and their bifurcations. *Adv. Appl. Mech.* **41**, 1–43.
- BRØNS, M., SHEN, W. Z., SØRENSEN, J. N. & ZHU, W. J. 2007 The influence of imperfections on the flow structure of steady vortex breakdown bubbles. *J. Fluid Mech.* **578**, 453–466.
- DE BRUIJN, N. G. 1970 *Asymptotic Methods in Analysis*. North-Holland.
- CHONG, M. S., PERRY, A. E. & CANTWELL, B. J. 1990 A general classification of three-dimensional flow fields. *Phys. Fluids* **A2** (5), 765–777.
- CIMBALA, H. M., NAGIB, H. M. & ROSHKO, A. 1981 Wake instability leading to new large scale structures downstream of bluff bodies. *Bull. Am. Phys. Soc.* **26**, 1256.
- CIMBALA, H. M., NAGIB, H. M. & ROSHKO, A. 1988 Large structure in the far wakes of two-dimensional bluff bodies. *J. Fluid Mech.* **190**, 265–298.
- DELERY, J. M. 1994 Aspects of vortex breakdown. *Prog. Aerospace Sci.* **30**, 1–59.

- DUSTING, J., SHERIDAN, J. & HOURIGAN, K. 2004 Flows within a cylindrical cell culture bioreactor with a free-surface and a rotating base. In *Proc. 15th Australasian Fluid Mechanics Conf.* (ed. M. Behnia, W. Lin & G. D. McBain). University of Sydney, Sydney, Australia, Paper No. AFMC00155.
- DUSTING, J., SHERIDAN, J. & HOURIGAN, K. 2006 A fluid dynamics approach to bioreactor design for cell and tissue culture. *Biotechnol. Bioengng* **94**, 1197–1208.
- FOUNTAIN, G., KHAKHAR, D. & OTTINO, J. 1998 Visualization of three-dimensional chaos. *Science* **281**, 683–686.
- GARDINER, C. W. 1985 *Handbook of Stochastic Methods*, 2nd edn. Springer.
- GELFGAT, A. Y. 2002 Three-dimensionality of trajectories of experimental tracers in a steady axisymmetric swirling flow: effect of density mismatch. *Theor. Comput. Fluid Dyn.* **16**, 29–41.
- GELFGAT, A. Y., BAR-YOSEPH, P. Z. & SOLAN, A. 1996 Stability of confined swirling flow with and without vortex breakdown. *J. Fluid Mech.* **311**, 1–36.
- GHONIEM, A. F. & SHERMAN, F. S. 1985 Grid-free simulation of diffusion using random walk methods. *J. Comput. Phys.* **61**, 1–37.
- GOLDSHTIK, M. & HUSSAIN, F. 1998 Analysis of inviscid vortex breakdown in a semi-infinite pipe. *Fluid Dyn. Res.* **23**, 189–234.
- GURSUL, I. & ROCKWELL, D. 1991 Effect of concentration of vortices on streakline patterns. *Exps. Fluids* **10**, 294–296.
- GURSUL, I., LUSSEYRAN, D. & ROCKWELL, D. 1990 On interpretation of flow visualization of unsteady shear flows. *Exps. Fluids* **9**, 257–266.
- HAMA, F. R. 1962 Streaklines in a perturbed shear flow. *Phys. Fluids* **5**, 644–650.
- HARTNACK, J. N., BRØNS, M. & SPOHN, A. 2000 The role of asymmetric perturbations in steady vortex breakdown bubbles. *DCAMM Rep.* 628. Technical University of Denmark.
- HOLMES, P. 1984 Some remarks on chaotic particle paths in time-periodic, three-dimensional swirling flows. *Contemporary Math.* **28**, 393–404.
- HOURIGAN, K., GRAHAM, L. W. & THOMPSON, M. C. 1995 Spiral streaklines in pre-vortex breakdown regions of axisymmetric swirling flows. *Phys. Fluids* **7** (12), 3126–3128.
- KLINE, S. J. 1969 National committee for fluid mechanics films, film notes for flow visualization. Publication 21607, Encyclopedia Britannica Educational Corporation, Chicago, Illinois.
- KRAUSE, E. & LIU, C. H. 1989 Numerical studies of incompressible flow around delta and double-delta wings. *Z. Flugwiss. Weltraumforschung* **13**, 291–301.
- KUROSAKA, M. & SUNDRAM, P. 1986 Illustrative examples of streaklines in unsteady vortices: interpretational difficulties revisited. *Phys. Fluids* **29** (10), 3474–3477.
- LEIBOVICH, S. 1978 The structure of vortex breakdown. *Annu. Rev. Fluid Mech.* **10**, 221–246.
- LEIBOVICH, S. 1984 Vortex stability and breakdown: survey and extension. *AIAA J.* **22**, 1192–1206.
- LEIBOVICH, S. 1999 Sensitivity of vortex flows and vortex breakdown to farfield conditions. In *AIAA 99-3765, 30th AIAA Fluid Dynamics Conf.*
- LIOW, K. Y. S., TAN, B. T., THOMPSON, M. C., HOURIGAN, K. & THOUAS, G. 2007 In-silico characterization of the flow inside a novel bioreactor for cell and tissue culture. In *Proc. 16th Australasian Fluid Mechanics Conf.* (ed. P. Jacobs, T. McIntyre, M. Cleary, D. Buttsworth, D. Mee, R. Clements, R. Morgan & C. Lemckert), pp. 361–367. School of Engineering, The University of Queensland.
- LOPEZ, J. M. & PERRY, A. D. 1992 Axisymmetric vortex breakdown. Part 3. Onset of periodic flow and chaotic advection. *J. Fluid Mech.* **234**, 449–471.
- OTTINO, J., LEONG, C., RISING, H. & SWANSON, P. 1988 Morphological structures produced by mixing in chaotic flows. *Nature* **333**, 419–425.
- RISKEN, H. 1989 *The Fokker–Planck Equation*. Springer.
- ROM-KEDAR, V., LEONARD, A. & WIGGINS, S. 1990 An analytical study of transport, mixing and chaos in an unsteady vortical flow. *J. Fluid Mech.* **214**, 347–395.
- RUSAK, Z. 1996 Axisymmetric swirling flow around a vortex breakdown point. *J. Fluid Mech.* **323**, 79–105.
- SOTIROPOULOS, F. & VENTIKOS, Y. 2001 The three-dimensional structure of confined swirling flows with vortex breakdown. *J. Fluid Mech.* **426**, 155–175.
- SOTIROPOULOS, F., VENTIKOS, Y. & LACKEY, T. C. 2001 Chaotic advection in a three-dimensional stationary vortex-breakdown bubble: Sil'nikov's chaos and the devil's staircase. *J. Fluid Mech.* **444**, 257–297.

- SOTIROPOULOS, F., WEBSTER, D. R. & LACKEY, T. C. 2002 Experiments on Lagrangian transport in steady vortex-breakdown bubbles in a confined swirling flow. *J. Fluid Mech.* **466**, 215–248.
- SPALL, R. E., GATSKI, T. B. & ASH, R. L. 1990 The structure and dynamics of bubble-type vortex breakdown. *Proc. R. Soc. Lond. A* **429**, 612–637.
- SPOHN, A., MORY, M. & HOPFINGER, E. J. 1998 Experiments on vortex breakdown in a confined flow generated by a rotating disc. *J. Fluid Mech.* **370**, 73–99.
- TAN, B. T., LIOW, K., HOURIGAN, K., SHERIDAN, J. & THOMPSON, M. C. 2006 Predicting the flow stresses in a simplified bioreactor. In *Proc. Eleventh Asian Congress of Fluid Mechanics* (ed. C. P. Tso, P. Viswanath, Y. Fukunishi & E. Cui), pp. 220–225. Kuala Lumpur, Malaysia.
- TANEDA, S. 1956 Experimental investigation of the wakes behind cylinders and plates at low Reynolds numbers. *J. Phys. Soc. Japan* **11**, 302–307.
- THOMPSON, M. C. & HOURIGAN, K. 2003 The sensitivity of steady vortex breakdown bubbles in confined cylinder flows to rotating lid misalignment. *J. Fluid Mech.* **496**, 129–138.
- THOUAS, G. A., SHERIDAN, J. & HOURIGAN, K. 2007 A bioreactor model of mouse tumor progression. *J. Biomed. Biotechnol.* Art. ID 32754, doi:10.1155/2007/32754.
- WILLIAMS, D. R. & HAMA, F. R. 1980 Streaklines in a shear layer perturbed by two waves. *Phys. Fluids* **23** (3), 442–447.
- YU, P., LEE, T. S., ZENG, Y. & LOW, T. H. 2005a Effect of vortex breakdown on mass transfer in a cell culture bioreactor. *Mod. Phys. Lett. B* **19**, 1543–1546.
- YU, P., LEE, T. S., ZENG, Y. & LOW, T. H. 2005b Fluid dynamics of a micro-bioreactor for tissue engineering. *Fluid Dyn. Mat. Process.* **1**, 235–246.
- YU, P., LEE, T. S., ZENG, Y. & LOW, T. H. 2007 Characterization of flow behaviour in an enclosed cylinder with a partially rotating end wall. *Phys. Fluids* **19**, 057104.
- ZIENKIEWICZ, O. C. 1977 *The Finite Element Method*, 3rd edn. McGraw-Hill.